Int. J. Electrochem. Sci., 14 **(2019)** 4995 – 5007, doi: 10.20964/2019.06.52

International Journal of
ELECTROCHEMICAL
SCIENCE
www.electrochemsci.org

Influence of Chloride Ions on Corrosion Behavior of Steel Bars in a Simulated Concrete Pore Solution

Hongwei Wu[1], *Keyu Pan*[1], *Yi Dai*[1], *Hesong Jin*[1], *Fuhai Li*[1,2,*]

[1] School of Civil Engineering, Southwest Jiaotong University, Chengdu 610031, China
[2] Key Laboratory of High-Speed Railway Engineering, Ministry of Education, Southwest Jiaotong University, Chengdu 610031, China
[*]E-mail: Lifuhai2007@home.swjtu.edu.cn

Received: 1 February 2019 / *Accepted:* 28 March 2019 / *Published:* 10 May 2019

The performance of steel bars deteriorates under chloride corrosion. It is thus essential to study the corrosion mechanism of different steel bars to better understand the corrosion of steel bars in concrete structures. In this study, electrochemical techniques and scanning electron microscopy are used to study different steel bars in a simulated concrete pore solution after different numbers of days. The findings suggest that each sample's free corrosion potential, impedance arc radius, and dispersion parameter decrease as the corrosion rate increases. When corrosion begins, the passive film remains unchanged, and one time constant is observed. Then, when the passive film is destroyed, two time constants appear. The pits exhibit a stepped structure with a discrete diameter and penetrate to the bottom of the passive layer. As the corrosion proceeds, the pits begin to overlap. The steel bar's fractal dimension first increases and then decreases. These results describe both the average characteristics and the details of the corrosion, providing theoretical guidance for choosing steel bars and monitoring corrosion.

Keywords: Steel bar corrosion; Polarization measurement; EIS; SEM; Fractal dimension;

1. INTRODUCTION

Reinforced concrete is employed in a variety of structures. According to previous research, one of the main factors affecting the durability of reinforced concrete is the corrosion of the steel bars [1]. When concrete structures are exposed to a high chloride content, such as in saline lakes and salinized soil areas, chloride ions can penetrate into the hardened concrete. Many studies have shown that chloride ion contents exceeding a threshold will destroy passive films and lead to corrosion [2-5]. However, the depassivation mechanism of chloride ions is still not clearly understood [6, 7].

The mechanism of corrosion has previously been studied [8]. Pitting nucleation usually begins at active corrosion sites and induces metastable micropitting. The growth of the micropits continues or

ceases depending on the local corrosion environment, the occurrence of repassivation, and the competition between micropits.

Alternating current (AC) and direct current (DC) methods are effective means for studying steel bar corrosion [9, 10]. Wang used these methods to evaluate the corrosion resistance of steel bars in a self-immunity system based on increasing the OH^- content [11]. Joiret observed that the sample spectrum of a passive film showed the presence of two time constants [12]. However, these methods also have some shortcomings in that they only detect the average state of sample corrosion. Corrosion is a random and complex process, and it thus cannot be simply described by AC and DC methods. Therefore, many researchers have used scanning electron microscopy (SEM) to observe the morphology as a supplement to electrochemical methods [13-20]. However, most of the results using SEM are qualitative, with limited quantitative information. Mandelbrot proposed fractal theory in the 20th century [21, 22], and fractal theory has proven to be a good tool for describing a complex process such as corrosion [23, 24]. After Costa utilized fractal theory to study the pitting profile of 316L stainless steel, it has been widely used in the evaluation of corrosion morphology [24]. Corrosion morphology is an important basis for judging various types of corrosion, evaluating corrosion levels, and studying corrosion laws and characteristics [25].

An experiment was carried out in a mixed solution of 5% NaCl, cement and $Ca(OH)_2$. AC/DC methods and SEM were comprehensively utilized. Moreover, fractal theory was applied to the SEM images. The behaviors of the steel bar corrosion were studied, and pure iron was used as a control group. This research provides essential insight into the evolution mechanisms of steel bars under chloride corrosion. In addition, these methodologies provide theoretical guidance for choosing steel bars and monitoring corrosion.

2. EXPERIMENTAL

2.1. Sample preparation

Nine cylindrical steel samples with a diameter of 10 mm and a length of 6 mm were prepared from pure iron (DT4) and two types of steel bars (HPB300 and HRB500). The composition of each sample is shown in **Table 1**. Each cross-sectional surface was polished to grade 1500 as the exposure surface and degreased in acetone. Then, the samples were derusted in oxalic acid, washed with distilled water, and cleaned in an ultrasonic bath. The resulting surface was sealed with epoxy resin, and a copper wire was soldered for testing.

Table 1. Compositional analysis of major elements in the pure iron (DT4) and steel bars (HPB300 and HRB500) used in this research (mass fraction, %)

Type	C	Si	Mn	S	P	Cr	Ni	Mo	V	Cu
DT4	0.0072	0.018	0.116	0.0050	0.012	0.010	0.0058	0.0052	0.0005	0.0027
HPB300	0.198	0.092	0.619	0.014	0.024	/	/	/	/	/
HRB500	0.232	0.432	1.30	0.011	0.019	0.022	0.0082	0.0029	0.027	0.031

2.2. Solution preparations

All chemical reagents in this experiment were of analytical grade. The samples were immersed in a saturated $Ca(OH)_2$ solution for 3 d before the experiment, as according to a previous study, a relatively stable passive film forms after 3 d of immersion [26]. The solutions used in the drying and watering cycles and the electrochemical tests were obtained by dissolving 20 g of 42.5R Portland cement (the oxide composition of the cement is shown in **Table 2**) in 2 L of 5% $NaCl$ and a saturated $Ca(OH)_2$ solution.

Table 2. Oxide composition of cement (%w/w)

Oxide	CaO	SiO_2	Al_2O_3	Fe_2O_3	Other	Ignition loss
% w/w	59.1	22.8	4.6	3.1	6.2	4.0

2.3. Experimental system and instruments

All electrochemical tests were performed in a three-electrode system in a Faraday box. The working electrodes were the pure iron and steel bars. The counter electrode was a platinum electrode with an area of 10 mm×10 mm, and the reference electrode was a saturated calomel electrode. Before the test began, the samples were immersed in the solution for half an hour to ensure that the open-circuit potentials (OCPs) were stable [27]. All electrochemical tests were performed using an Autolab PGSTAT302N.

2.4. Polarization measurement

The OCPs were recorded before the polarization measurements began, and all polarization measurements were related to the OCP. The sample reached a relatively stable condition after immersion in the testing solution for 30 minutes. Then, scanning began in the range from -0.2 V to 0.1 V relative to the OCP at a scan rate of approximately 0.002 V/s. Tafel extrapolation and the Butler-Volmer equation were used to obtain i_{corr}, E_{corr}, b_a and b_c.

2.5. Electrochemical impedance spectroscopy (EIS)

Electrochemical impedance spectroscopy (EIS) was carried out at the OCP with an amplitude of 20 mV and a sweep frequency of 100 kHz to 10 mHz.

2.6. Analysis and fractal characteristics of the SEM images

The morphology of the samples was observed by a KYKY-EM3200 scanning electron microscope. The fractal dimensions of the grayscale SEM images were calculated by the box-counting

algorithm. The box-counting dimension of a compact set A in R^n is defined as follows. R^n can be divided into ε-cubes by a grid based on, for example, points whose coordinates are ε-multiples of integers. Let $N(\varepsilon)$ be the number of boxes that intersect A. If the upper box-counting dimension is equal to the lower dimension, then [28]

$$\text{boxdim}(A)=\lim_{\varepsilon\to 0}\frac{\log N(\varepsilon)}{-\log(\varepsilon)} \quad (2)$$

The scaling in this case is

$$N(\varepsilon)\approx\varepsilon^{-d} \quad (3)$$

The box-counting algorithm was applied in ImageJ.

3. RESULTS AND DISCUSSION

3.1. Polarization measurement

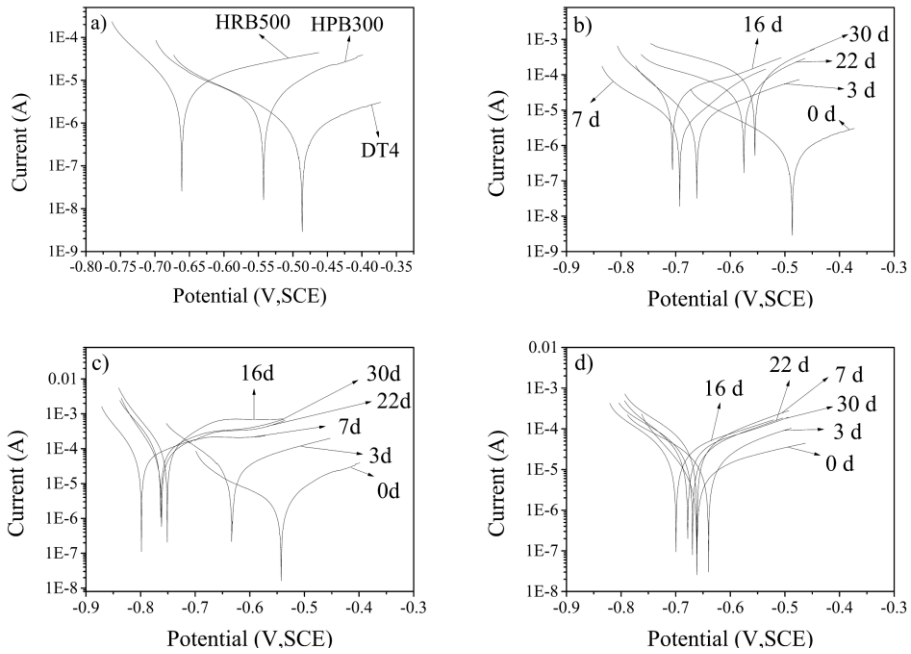

Figure 1. a) Polarization curves of different samples on day 0; b), c), d) polarization curves of samples DT4, HPB300 and HRB500 at different immersion times.

Fig. 1 a) shows the polarization curves of the samples in the test solution on day 0. Each curve contains a cathodic and an anodic polarization branch, commonly used for material electrochemical characteristic recognition. A rapid increase in current is observed in the weakly polarized area. This increase indicates that the anode process is initially controlled by activation [29]. In addition, the cathodic reaction shows concentration control. In the strongly polarized region (also known as the Tafel region), the curve is quite flat, which indicates that the corrosion mechanism of the sample does not change. The anodic polarization currents show the corrosion resistance of the steel bars. HRB500 and HPB300 are susceptible to corrosion; HRB500 is more susceptible than HPB300 in the beginning. **Figs**.

1 b), c), and d) show the polarization curves of each sample in the test solution on different days. For each sample, the increase in the anodic polarization current was obvious in the beginning. After 7 d, the increase in the anode current slowed and began to fluctuate, and the OCP values fluctuated around the 7-d OCP.

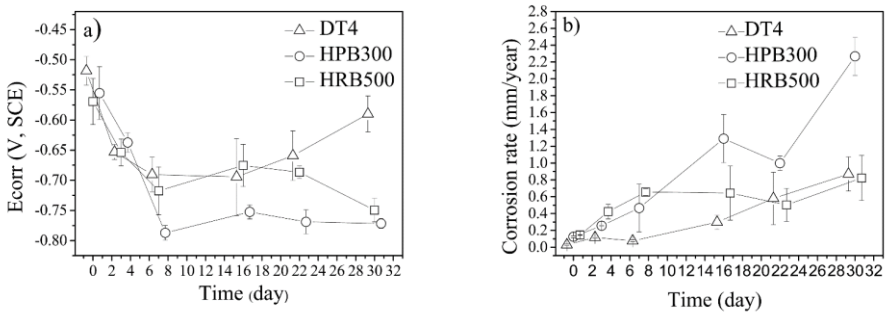

Figure 2. a), b) Average free corrosion potentials/corrosion rates of DT4, HPB300, and HRB500 in the 5% $NaCl$, saturated $Ca(OH)_2$ and cement solutions at different immersion times.

The free corrosion potential is measured in the absence of a net electrical current that flows to or from a metal's surface. The corroding metal has a potential that is expressed as E_{corr}, and this parameter is a thermodynamic indicator. The lower the corrosion potential is, the greater the tendency for corrosion. **Fig. 2** a) shows the average free corrosion potentials of DT4, HPB300, and HRB500 in the 5% $NaCl$, saturated $Ca(OH)_2$ and cement solutions. As the time progressed, each sample's corrosion resistance showed a significant downward trend. After 7 d, all samples' E_{corr} fluctuated within a certain range. For the different samples, at the beginning, the potentials were close to each other. After 30 d, DT4 showed the largest corrosion resistance. The resistance of HRB500 was stronger than that of HPB300, which may be due to the presence of alloying elements, such as Mn, Si, and Cr. Although HRB500 contains more carbon than the other samples, the contents of Mn, Si, and Cr are also higher. According to the literature [30, 31], elements such as P, Si, Cr, Cu, Co, and Ni can improve the corrosion resistance of steel. Therefore, HRB500 exhibits a stronger corrosion resistance.

The corrosion rate is the speed at which a metal in a specific environment deteriorates. It can be defined as the amount of corrosion loss per year in terms of thickness, which can be determined by the following formula:

$$d = \frac{\upsilon}{\rho} = 3.28\times10^{-3}\frac{M}{n\rho}\,j_{corr} \qquad (4)$$

In this experiment, M=56, n=2, and ρ =7.8 g/cm2, where j_{corr} is the current density ($\mu A/cm^2$).

Fig. 2 b) shows the average corrosion rates of DT4, HPB300, and HRB500 in the test solutions. All corrosion rates were greater than 0.01 mm/year at the beginning of the test. Therefore, the 5% chloride ion concentration is highly corrosive to the steel bars and pure iron. As the test time progressed, the corrosion rates of the samples increased significantly. The error bars at the beginning of the

experiment were smaller than those later in the experiment, which indicates that corrosion is a random and complex process. Among the different samples, in the beginning, HPB300 and HRB500 exhibited much higher corrosion rates than DT4. The corrosion resistance of HPB300 and HRB500 is thus weaker than that of DT4. By the 16th day, the corrosion rate of HPB300 exceeded that of HRB500, which showed that HPB300 is more prone to corrosion. This result is consistent with the free corrosion potential results.

3.2. Electrochemical impedance spectroscopy (EIS)

Fig. 3 a) shows the Nyquist plots of the samples on day 0, and **Figs. 3** b), c), and d) show the Nyquist plots of DT4, HPB300 and HRB500, respectively, on different days. All the Nyquist plots had a semicircular arc with a large radius at the beginning. As the corrosion progressed, the radius of the semicircular arc gradually decreased. The semicircular dip angles caused by the dispersion effect also increased over time. The diffusion effect caused the high-frequency capacitance to exhibit a squashed capacitive reactance arc rather than a regular semicircle. This pattern occurred because corrosion makes steel surfaces uneven [32, 33]. As shown in **Fig. 3** a), among the studied samples, DT4 has the largest semicircle radius and the smallest dispersion angle, while HRB500 has the smallest radius and the largest dispersion angle.

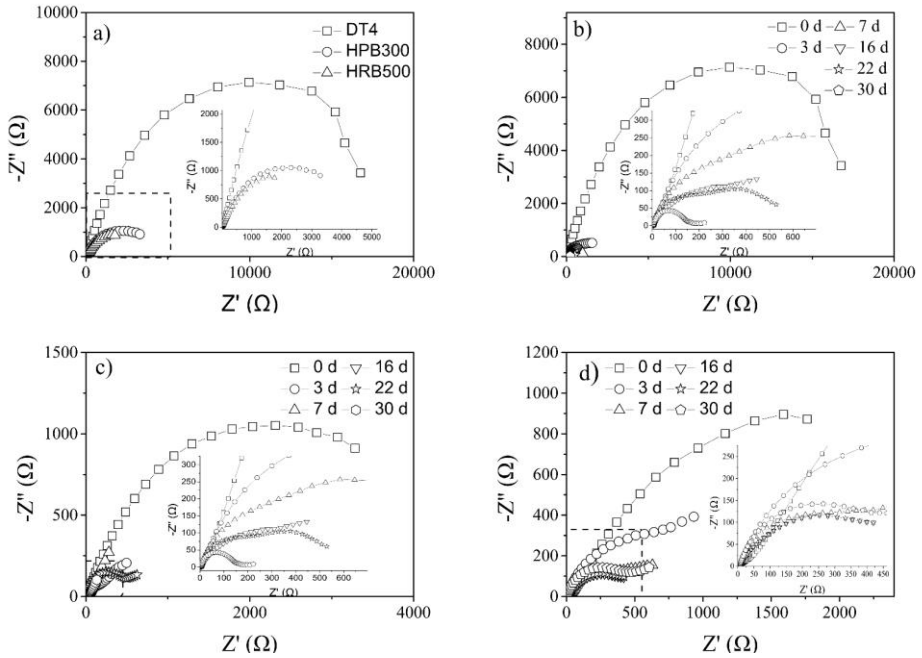

Figure 3. a) Nyquist plots of the samples on day 0; b), c), d) DT4, HPB300 and HRB500 Nyquist plots on different days.

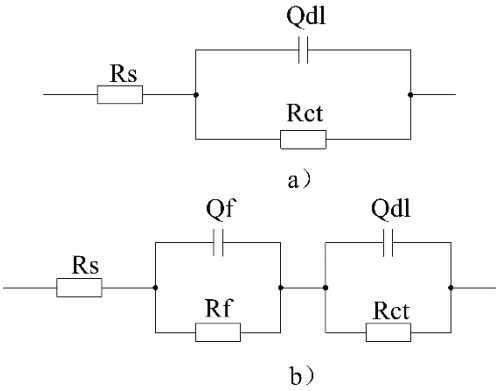

Figure 4. a) Equivalent circuit of reinforcing steel with passive film immersed in simulated solutions. b) Equivalent circuit of reinforcing steel without a passive film immersed in simulated solutions.

The semicircle radius of HPB300 was slightly larger than that of HRB500. This result indicates that HRB500 is the most susceptible to corrosion in the beginning and that the corrosion resistance of HPB300 was slightly larger than that of HRB500 in the beginning, which is consistent with the polarization measurement on day 0. As time passed, the semicircular arc became irregular, and the radius decreased. According to previous research, the reason for this result may be the surface deposition of corrosion products, which may affect the charge and discharge processes. As the corrosion continued, the rust layer thickened, and the capacitance increased [34, 35]. The equivalent circuit model can help us obtain a better understanding of the corrosion behavior. Therefore, a simulation analysis of the equivalent circuit model was carried out to obtain the charge transfer resistance R_{ct} , the constant phase element (CPE) and other circuit parameters. In the simulation theory, the Nyquist plot of high frequencies represents the electrolyte resistance and the interface resistance of the steel bars and the electrolyte. The low-frequency part represents the charge transfer resistance, which is equal to R_{ct} . Similar to the literature [36], the equivalent circuit model shown in **Fig. 4** a) was applied to analyze the EIS data in the early stage of the experiment to obtain parameters such as R_{ct} . In this equivalent circuit, R_s is the electrolyte resistance, and R_{ct} represents the charge transfer resistance. The double-layer capacitor Q_{dl} value is determined using a CPE representing a nonideal frequency-dependent capacitance. The CPE is derived from the following formula:

$$Y_{CPE}=Y_0(i\omega)^n \quad (5)$$

where n is a value between 1 and 0.5 and describes the frequency domain of the distribution of the dielectric relaxation time. For $n=0$, the CPE is a resistor, and for $n=1$, the CPE is a capacitor. The presence of the CPE may result from the fractal properties of the electrode interface at the steel bar surface or heterogeneity in the steel bars.

The concave shape of the capacitive reactance arc can be clearly observed in **Figs. 3** b), c), and d). Two capacitive reactance arcs also appeared afterwards. The high-frequency capacitive reactance arc indicates the electric double-layer behavior between the passive film on the sample surface and the solution, which represents the dissolution of the steel bar's passive film. The medium- to low-frequency capacitive arc corresponds to the dissolution process of the steel bar substrate under the passive film layer. In this case, the equivalent circuit model was revised for **Fig. 4** b). R_f and Q_f are the resistance

and capacitance of the passive film on the sample surface, respectively. CPE2 is substituted for the Q_f value. R_{ct} and Q_{dl} represent the charge transfer resistance and the double-layer capacitance of the electrode/electrolyte interface, respectively. The Q_{dl} value is obtained by CPE1.

At the beginning of the corrosion, the passive film was undamaged. One time constant was displayed, and the fitting circuit is shown in **Fig. 4** a). When the passive film was later damaged, two time constants appeared, as shown in **Fig. 4** b), indicating that the passive film was partly dissolved. After 7 d, the capacitive reactance arcs became closer, indicating that the sample was entering a relatively stable corrosion condition, which is consistent with the polarization measurement results.

3.3. Analysis of the SEM images

Fig. 5 shows SEM images (2,000× magnification) of DT4 on different days. The surface only showed polishing scuffing on day 0. After 3 d, two pits with diameters of approximately 10 μm appeared. Then, the pits became larger, but the depth did not increase significantly relative to those in HPB300 and HRB500.

Fig. 6 shows SEM images (2,000× magnification) of HRB500 on different days. At the beginning, the surface showed the same polishing scuffing as in the SEM images of DT4. After 3 d, a corrosion pit with a diameter of approximately 20 μm appeared. The area near the pit became rougher due to the dissolution of steel. On the 16th day, two corrosion pits overlapped. The corrosion pit on the right side had a stepped layer with a discrete diameter and penetrated to the bottom of the passive layer. Therefore, each corrosion pit appeared to be independent of the others. Once the corrosion intensifies, pits are likely to overlap, which is consistent with previously published research [37]. On the 30th day, the pit had a larger diameter. The external diameter was approximately 41.8 μm, and the internal diameter was approximately 22.3 μm. The change in diameter was progressive. **Fig. 7** shows SEM images (2,000× magnification) of HPB300 on different days.

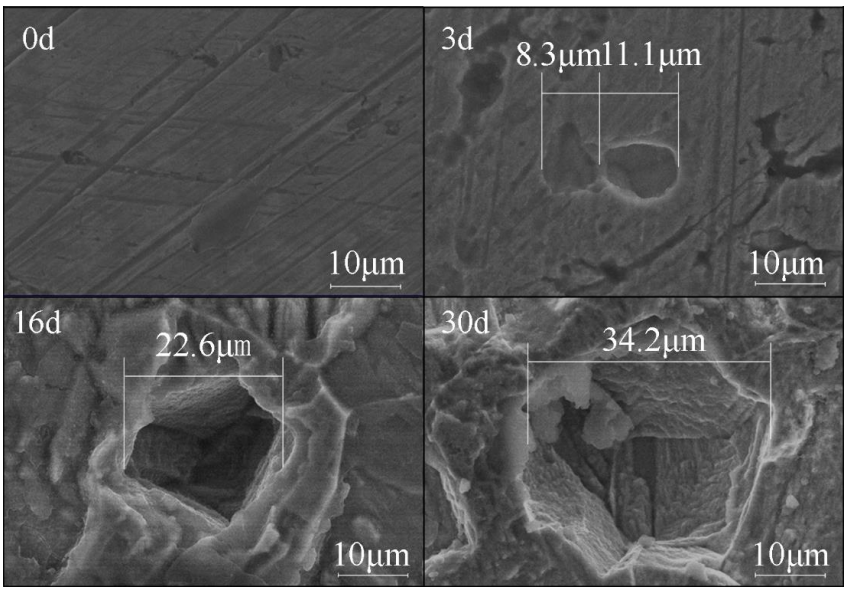

Figure 5. DT4 SEM images (2000× magnification) on different days.

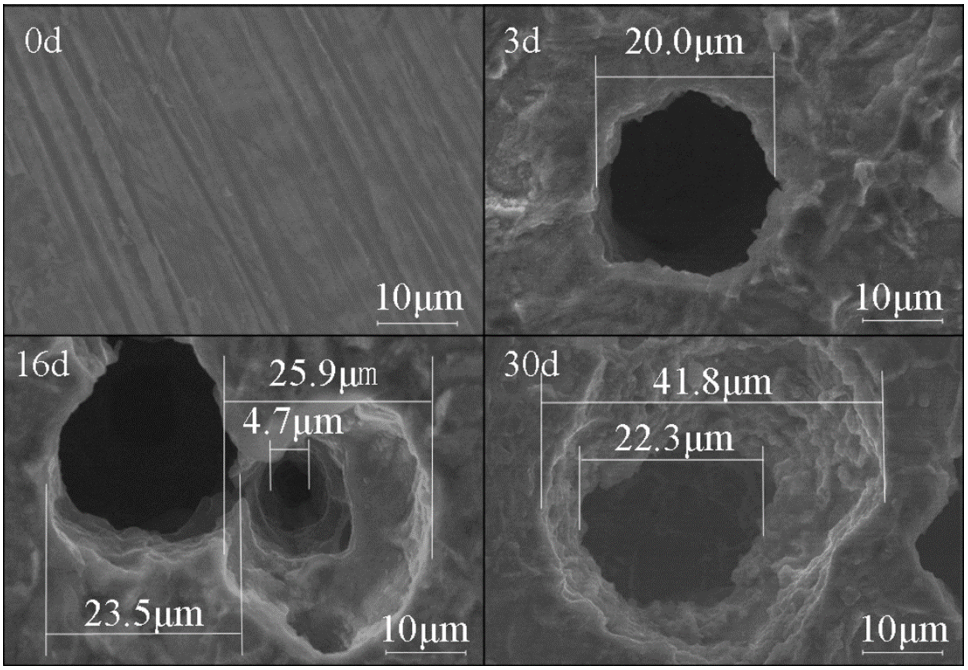

Figure 6. HRB500 SEM images (2000× magnification) on different days.

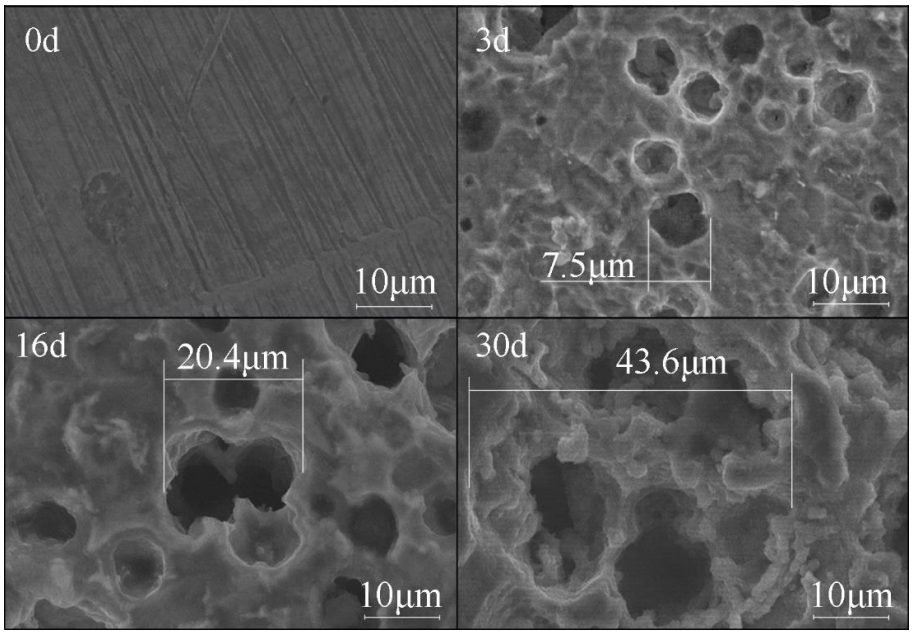

Figure 7. HPB300 SEM images (2000× magnification) on different days.

The overlap between two corrosion pits can also be seen in HPB300. In addition, the pits in HPB300 were numerous and had small radii, while the pits in HRB500 were fewer in number but larger in radius. Therefore, different corrosion mechanisms exist in HRB500 and HPB300.

Based on the analysis of the SEM images, the pure iron DT4 has a different corrosion mechanism from that of the steel bars. The pits of DT4 extend farther horizontally, while the pits of HPB300 and HRB500 extend deeper into the surface.

3.4. Fractal characteristics of the SEM images

The fractal dimension was correlated with the magnification power of the SEM images. A higher magnification power resulted in a lower fractal dimension. From the data from the HRB500 SEM images of 22 d and 30 d, an exponential relationship can be observed. Thus, the logarithmic data of the magnification power were used to fit the fractal dimension, as shown in Fig. 6. The reason for this is that the difference in similarity is hierarchical. A previous study found similar results [38]. Therefore, to make the fractal dimensions of the samples comparable, the same magnification must be selected.

Grayscale images at a magnification power of 500 were used to calculate the fractal dimensions in this paper. An SEM image (**Fig. 8**) shows the morphology of the DT4 and HPB300 surfaces at a magnification power of 500. The samples appear different as a result of the different corrosion durations and compositions.

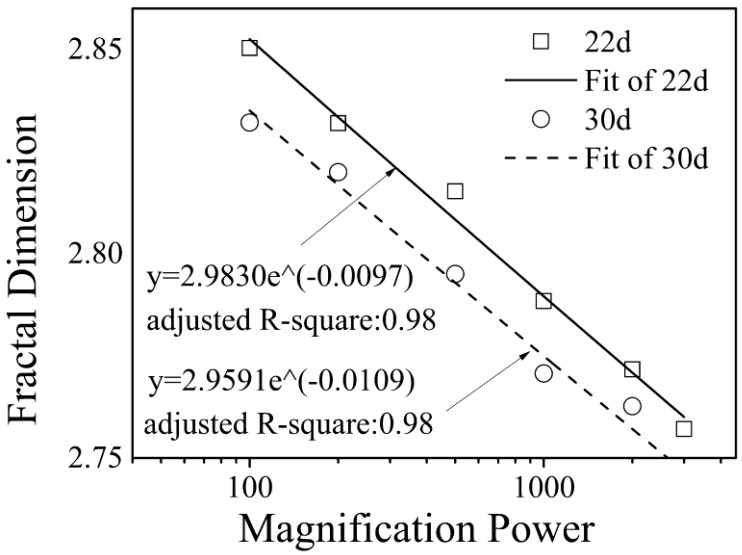

Figure 8. The fitting curve of the fractal dimensions and magnification powers.

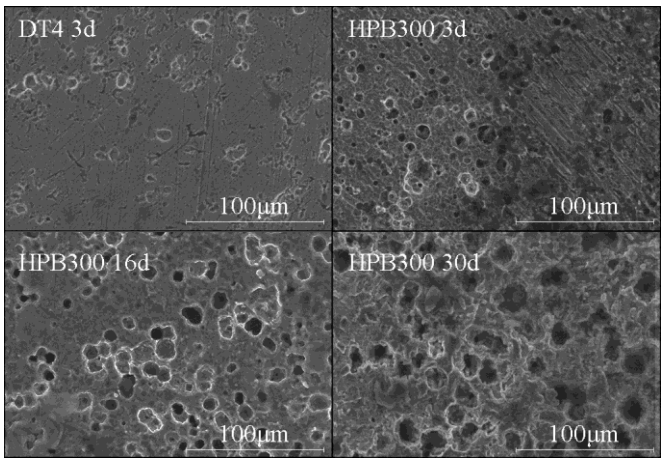

Figure 9. Different sample surface characteristics imaged via SEM (500× magnification) on different days.

The topographical differences between different samples can be reflected using fractal dimensions. The fractal dimensions extracted from the SEM images (**Fig. 9**) of the different samples are as follows: $D_1 = 2.7793$ (DT4 after 3 d), $D_2 = 2.8084$ (HPB300 after 3 d), $D_3 = 2.8232$ (HPB300 after 16 d) and $D_4 = 2.8035$ (HPB300 after 30 d). The fractal dimension of DT4 (after 3 d) is lower than that of HPB300 (after 3 d), indicating that HPB300 has a lower corrosion resistance. For HPB300, in the early stage, as the corrosion proceeded, the surface of the steel bar became rougher, and the pits began to grow, which increased the fractal dimension. The fractal dimension of HPB300 increased from 2.8084 to 2.8232. On the 16th day, the surface of HPB300 was rougher, and more pits had formed. Then, the dimension decreased to 2.8035 after 30 days. This change reflected the process of the dissolution of peaks. As the surface became flatter, the fractal dimension decreased, which is consistent with previous research [39].

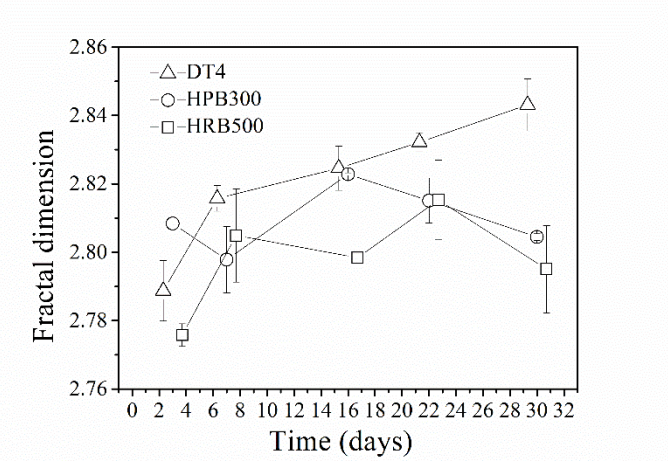

Figure 10. The fractal dimensions of the different samples on different days.

Fig. 10 shows the changes in the fractal dimensions of the samples during the experiment. For HPB300 and HRB500, the fractal dimensions of the samples first increased and then decreased for the same reason as stated in the previous paragraph. However, the fractal dimension change in DT4 is more difficult to determine; the fractal dimension was not lower on the 30th day. This difference may be related to the different mechanism of DT4 corrosion. An analysis of the SEM images reveals that the corrosion pits in the pure iron tend to extend horizontally. Additionally, DT4 is resistant to corrosion. Therefore, it may take more time for the DT4 fractal dimension to begin to decrease. From the results of the fractal characteristics, the fractal dimension changes in the same sample are easily observed and can be used for corrosion monitoring. However, this method is not suitable for comparisons between different samples.

4. CONCLUSION

The corrosion behavior of steel bars exposed to chloride ions was investigated in simulated concrete pore solutions. Electrochemical measurements and SEM were utilized in combination to

evaluate the corrosion of the steel bars, and fractal theory was applied to the SEM images. The following conclusions were obtained:

1) To obtain a good understanding of corrosion mechanisms, polarization, EIS and SEM should be mutually utilized to observe the process of corrosion. These methods can also be used to monitor corrosion or evaluate the corrosion resistance of steel bars in concrete structures in chlorine-rich environments.

2) As corrosion progresses, the free corrosion potential of pure iron and steel bars decreases as the corrosion rate increases. Meanwhile, the radius of the impedance arc and the dispersion parameter decrease. After 7 d, the decreases in the free corrosion potential, the radius of the impedance arc, and the dispersion parameter slow. The corrosion has then entered a relatively stable phase in the experimental environment. The equivalent circuit model of steel bars differs at different stages of corrosion. The Nyquist plot shows one time constant before the reinforced passive film is damaged. After the passive film is damaged, two time constants are observed.

3) The corrosion pits have a stepped structure with a discrete diameter and penetrate the bottom of the passive layer. With continued corrosion, the pits exhibit progressively larger diameters. Additionally, as the corrosion progresses, more pits appear and begin to overlap.

4) The pits in DT4 tend to extend horizontally, while the pits in HPB300 and HRB500 tend to extend deeper into the surface. The pits in HPB300 were numerous and had small radii, whereas the pits in HRB500 were less abundant but had larger radii.

5) As corrosion proceeds, the fractal dimensions of the steel bars first increase and then decrease. The fractal dimensions are higher for rougher surfaces with more pits. However, as the surfaces become flatter due to the dissolution of peaks, the dimensions decrease.

ACKNOWLEDGMENTS

The authors gratefully acknowledge the financial support from the Natural Science Foundation of China No. 51308471, the National Undergraduate Innovative Experimental Program No. 201810613008 and the Southwest Jiaotong University Personalized Experiment No. GX201812120.

References

1. P.K. Mehta, Durability of concrete-fifty years of progress, *Proceedings of the 2nd International Conference on Concrete Durability*, Montreak, Canada, 1991, 1.
2. J. Xu, L. Jiang and J. Wang, *Constr. Build. Mater.*, 23 (2009) 1902.
3. L. Jiang, G. huang, J. Xu, Y. Zhu and L. Mo, *Constr. Build. Mater.*, 30 (2012) 516.
4. G. Liu, Y. Zhang, Z. Ni and R. Huang, *Constr. Build. Mater.*, 115 (2016) 1.
5. J. Soltis, *Corros. Sci.*, 90 (2015) 5.
6. F.J. Martin and J. Olek, *Rev. Sci. Instrum.*, 74 (2003) 2512.
7. V. Kumar, *Corros. Rev.*, 16 (1998) 317.
8. C. Wang, Y. Cai, C. Ye, S. Dong, X. Cai, Y. Cao and C. Lin, *Electrochem. Commun.*, 90 (2018) 11.
9. Y. Wang, G. Cheng, W. Wu, Q. Qiao, Y. Li and X. Li, *Appl. Surf. Sci.*, 349 (2015) 746.
10. Z. Ai, J. Jiang, W. Sun, D. Song, H. Ma, J. Zhang and D. Wang, *Appl. Surf. Sci.*, 389 (2016) 1126.
11. Y. Wang, W. Ding, G. Fang, Y. Liu, F. Xing and B. Dong, *Constr. Build. Mater.*, 125 (2016) 742.
12. M.K.S. Joiret, X.R. Novoa, M.C. Perez, C. Rangel and H. Takenouti, *Cem. Concr. Compos.*, 24

(2002) 7.
13. H. Duan, K. Du, C. Yan and F. Wang, *Electrochim. Acta*, 51 (2006) 2898.
14. W. Li, Q. He, S. Zhang, C. Pei and B. Hou, *J. Appl. Electrochem.*, 38 (2007) 289.
15. M.A. Amin, S.S. Abd El-Rehim, E.E.F. El-Sherbini and R.S. Bayoumi, *Electrochim. Acta*, 52 (2007) 3588.
16. R. Solmaz, G. Kardaş, M. Çulha, B. Yazıcı and M. Erbil, *Electrochim. Acta*, 53 (2008) 5941.
17. A. Ostovari, S.M. Hoseinieh, M. Peikari, S.R. Shadizadeh and S.J. Hashemi, *Corros. Sci.*, 51 (2009) 1935.
18. M.A. Jingling, W. Jiuba, L.I. Gengxin and X.V. Chunhua, *Corros. Sci.*, 52 (2010) 534.
19. B. Hamah-Ali, B.S. Ali, R. Yusoff and M.K. Aroua, *Int. J. Electrochem. Sci.*, 6 (2011) 181.
20. S.S. Golru, M.M. Attar and B. Ramezanzadeh, *J. Ind. Eng. Chem.*, 24 (2015) 233.
21. B.B. Mandelbrot, D.E. Passoja and A.J. Paullay, *Nature*, 308 (1984) 721.
22. B.B. Mandelbrot, *Fractals: Form, Chance, and Dimension*, W. H. Freeman, **US** (1977).
23. R. Lopes and N. Betrouni, *Med Image Anal*, 13 (2009) 634.
24. J.M. Costa, F. Sagues and M. Vilarrasa, *Corros. Sci.*, 32 (1991) 665.
25. F.A. Champion, *Corrosion testing procedure*, Chapman and Hall, **UK** (1964).
26. A. Poursaee and C.M. Hansson, *Cem. Concr. Res.*, 37 (2007) 1127.
27. V. Padilla and A. Alfantazi, *Constr. Build. Mater.*, 66 (2014) 447.
28. T. Sauer, J.A. Yorke and M. Casdagli, *J. Stat. Phys.*, 65 (1991) 579.
29. N.R. Short, A. Abibsi and J.K. Dennis, *Trans. IMF*, 67 (2017) 73.
30. H. Baorong, Z Jinglei, W. Jia and X. Xiaobo, *Stu. Mari. Sin.*, 36 (1995).
31. G. Fu, M. Zhu, X. Gao, *Mater. Sci.*, 22 (2016).
32. Z.Lukács, *J. Electroanal. Chem.*, 464 (1999) 68.
33. Z.Lukács, *J. Electroanal. Chem.*, 432 (1997) 79.
34. B. Panda, R. Balasubramaniam and G. Dwivedi, *Corros. Sci.*, 50 (2008) 1684.
35. L. Bousselmi, C. Fiaud, B. Tribollets and E. Trikis, *Corros. Sci.*, 39 (1997) 1711.
36. L. Li and A.A. Sagüés, *Corrosion*, 57(2001) 19.
37. J.Y. Jiang, Y. Liu, H.Y. Chu, D. Wang, H. Ma and W. Sun, *Material*, 18 (2017) 903.
38. H.P. Tang, J.Z. Wang, J.L. Zhu, Q.B. Ao, J.Y. Wang, B.J. Yang and Y.N. Li, *Powder Technol.*, 217 (2012) 383.
39. D. Risović, S.M. Poljaček, K. Furić and M. Gojo, *Appl. Surf. Sci.*, 255 (2008) 3063.